Hereditary parkinsonism with dementia is caused by mutations in *ATP13A2*, encoding a lysosomal type 5 P-type ATPase

Alfredo Ramirez[1–4], André Heimbach[1–3], Jan Gründemann[5], Barbara Stiller[1–3], Dan Hampshire[6], L Pablo Cid[7], Ingrid Goebel[1–4], Ammar F Mubaidin[8], Abdul-Latif Wriekat[8], Jochen Roeper[5], Amir Al-Din[9], Axel M Hillmer[4,10], Meliha Karsak[11], Birgit Liss[5], C Geoffrey Woods[12], Maria I Behrens[13] & Christian Kubisch[1–4]

Neurodegenerative disorders such as Parkinson and Alzheimer disease cause motor and cognitive dysfunction and belong to a heterogeneous group of common and disabling disorders[1]. Although the complex molecular pathophysiology of neurodegeneration is largely unknown, major advances have been achieved by elucidating the genetic defects underlying mendelian forms of these diseases[2]. This has led to the discovery of common pathophysiological pathways such as enhanced oxidative stress, protein misfolding and aggregation and dysfunction of the ubiquitin-proteasome system[3–6]. Here, we describe loss-of-function mutations in a previously uncharacterized, predominantly neuronal P-type ATPase gene, *ATP13A2*, underlying an autosomal recessive form of early-onset parkinsonism with pyramidal degeneration and dementia (PARK9, Kufor-Rakeb syndrome[7,8]). Whereas the wild-type protein was located in the lysosome of transiently transfected cells, the unstable truncated mutants were retained in the endoplasmic reticulum and degraded by the proteasome. Our findings link a class of proteins with unknown function and substrate specificity[9] to the protein networks implicated in neurodegeneration and parkinsonism.

Kufor-Rakeb syndrome (KRS) is a rare hereditary disease with juvenile onset and unknown cause. In addition to typical signs of Parkinson disease, affected individuals show symptoms of more widespread neurodegeneration, including dementia[7,8]. The disease locus has been previously linked to a 9-cM region on chromosome 1p, within a cluster of early-onset Parkinson disease loci[10]. We identified a large non-consanguineous Chilean family with early-onset Parkinson disease resembling the original KRS family (**Supplementary Note** online). By mutation screening or linkage analysis, we excluded the known autosomal recessive Parkinson disease genes and loci: *PARK2* (also known as *Parkin*; ref. 11), *PARK7* (also known as *DJ-1*; ref. 12) and *PARK6* (also known as *PINK1*; ref. 13). However, between *PARK7* and *PARK6*, we found linkage to a 23-cM region bordered by *D1S2736* and *D1S2644* (**Fig. 1**). The maximum two-point and multipoint lod scores were 2.68 (**Supplementary Table 1** online) and 3.68, respectively. This finding reduced the critical KRS interval to a 6.6-cM region spanning 3.2 Mb and harboring around 40 known genes, without an obvious functional candidate. After exclusion of *IGSF21*, we sequenced all 29 exons and splice sites of the predicted gene *ATP13A2* (primer sequences in **Supplementary Table 2** online) and identified two different mutations in a compound heterozygous state in all affected individuals. The first mutation (also present in the mother; on the red haplotype in **Fig. 1**) is a deletion of a cytosine at nucleotide position 3057 in exon 26 leading to a frameshift and stop codon after two extraneous amino acids (3057delC or 1019GfsX1021; **Fig. 2a**). The second mutation (inherited from the father; on the yellow haplotype in **Fig. 1**) is a guanine-to-adenine transition at position +5 of the donor splice site of exon 13 (1306+5G→A; **Fig. 2a**). This mutation of a highly conserved splice site residue is predicted to strongly impair splicing efficacy, dropping from 0.98 to 0.11 (http://www.fruitfly.org). Indeed, cDNA amplification on blood samples with primers in exons 12 and 14 uncovered an aberrant smaller fragment in the father and two affected children that was not present in the mother or in control cDNA from human brain (**Fig. 2b**). Sequencing of the aberrant band uncovered in-frame skipping of exon 13 (removing 111 nucleotides) caused by the splice site mutation (**Fig. 2b**). To confirm the causative role of *ATP13A2* mutations in KRS, we performed mutation screening in the originally

[1]Institute of Human Genetics, [2]Institute for Genetics and [3]Center for Molecular Medicine Cologne, University of Cologne, 50931 Cologne, Germany. [4]Institute of Human Genetics, University of Bonn, 53111 Bonn, Germany. [5]Institute of Physiology, University of Marburg, 35037 Marburg, Germany. [6]Molecular Medicine Unit, University of Leeds, Leeds LS9 7TF, UK. [7]Centro de Estudios Científicos (CECS), Valdivia 509-9100, Chile. [8]Neurology Department, King Hussein Medical Centre, Amman 11947, Jordan. [9]Department of Neurology, Pinderfields Hospital, Wakefield WF1 4DG, UK. [10]Department of Genomics and [11]Department of Molecular Psychiatry, Life and Brain Center, University of Bonn, 53127 Bonn, Germany. [12]Cambridge Institute for Medical Research, Cambridge CB2 2QQ, UK. [13]Department of Neurology and Neurosurgery, University of Chile, Santiago 820-7257, Chile. Correspondence should be addressed to C.K. (christian.kubisch@uk-koeln.de).

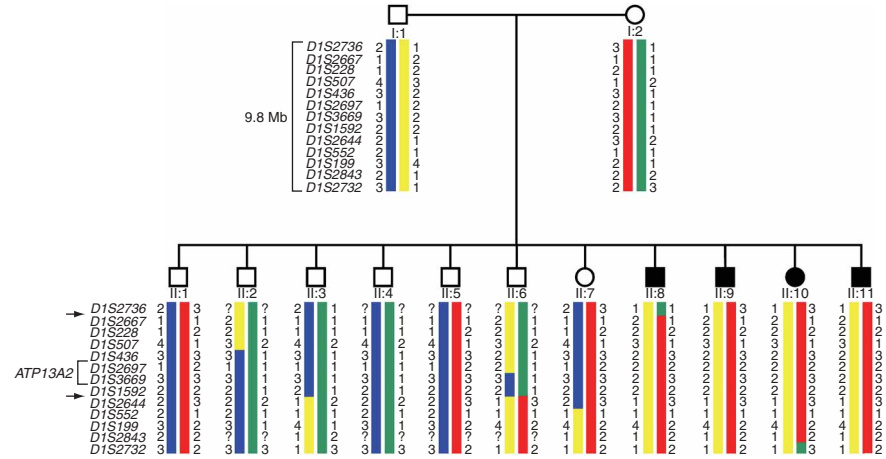

Figure 1 Haplotype analysis of the KRS-locus on chromosome 1p in the Chilean family. Affected family members are shown in black; circles and squares denote female and male individuals, respectively. The microsatellite markers are given on the left, and the location of *ATP13A2* is indicated by the small bracket. Critical recombinations in II:8 (telomeric) and II:6 (centromeric) are shown by arrows. All affected family members are compound heterozygous for the paternal (yellow) and maternal (red) haplotypes in the critical KRS interval.

described Jordanian KRS family. Analysis of exon 16 showed a homozygous 22-bp duplication in all affected family members (1632_1653dup22 or 552LfsX788; **Fig. 2c**) leading to a frameshift and stop codon after 236 extraneous amino acids. All mutations cosegregated with the disease and were not found in 480 German control chromosomes.

ATP13A2 codes for a member of the P-type ATPase superfamily[9,14] with its characteristic ten-transmembrane domain topology (**Fig. 2d**). The two frameshift mutations remove the three or six C-terminal transmembrane domains, respectively (**Fig. 2d**), which is expected to cause a loss of function. The in-frame skipping of exon 13 removes 37 amino acids, including half of the third transmembrane domain (**Fig. 2d**). The remaining hydrophobic residues of this domain will not be able to span the membrane, which should lead to a distortion of transmembrane topology and also to loss of function.

We defined the human gene sequence by cDNA amplification and RACE, as *ATP13A2* has been predicted only on the basis of EST and homology data[15,16]. The ORF consists of 3,543 nucleotides coding for

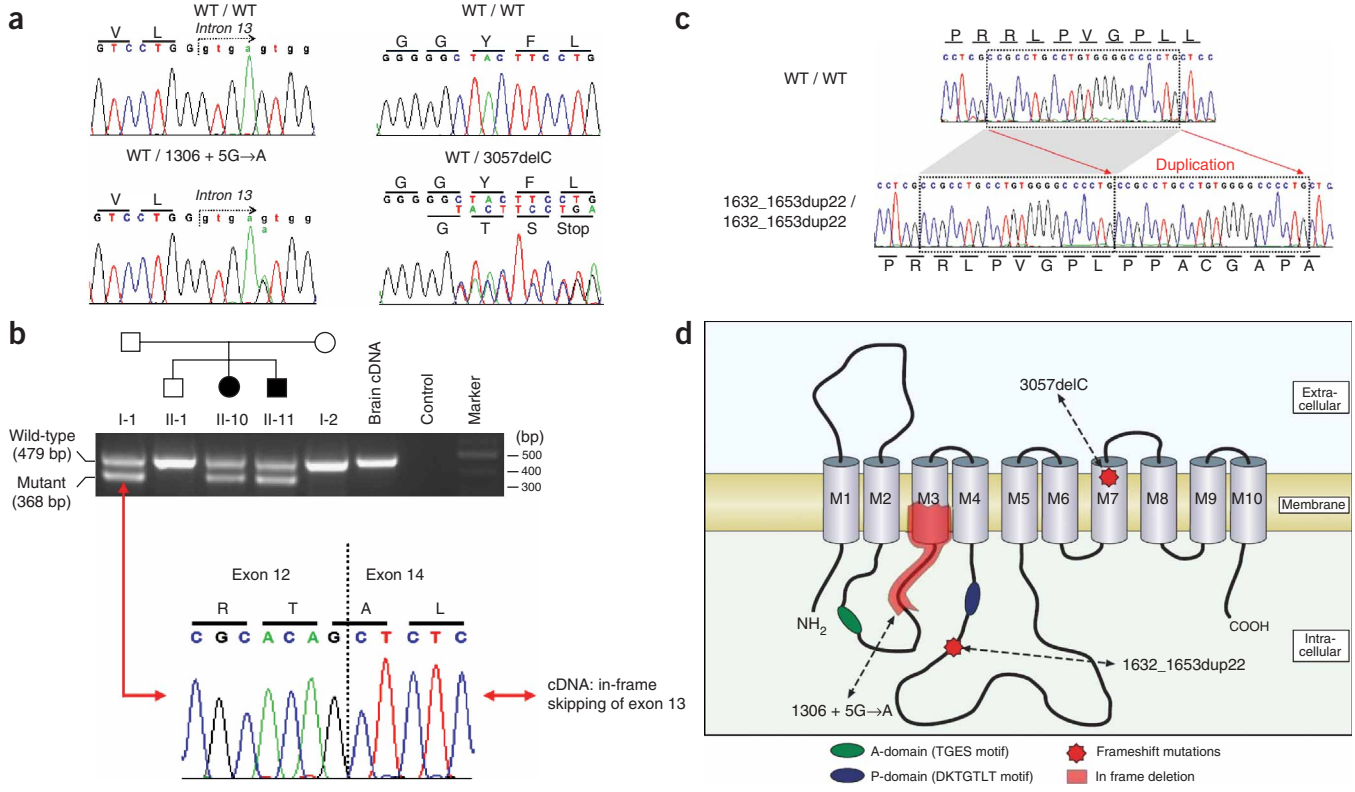

Figure 2 *ATP13A2* mutations in individuals with KRS and their predicted effect on the protein structure. (**a**,**c**) Direct sequencing of mutation carriers and controls in the Chilean family (**a**) and the original KRS family[10] (**c**). Wild-type (WT) sequences and amino acid translations are shown above; mutations are shown below. The Chilean individuals are compound heterozygous for 1306+5G→A and 3057delC, and the Jordanian patients are homozygous for 1632_1653dup22. (**b**) RT-PCR analysis of the 1306+5G→A mutation. Exons 12–14 of *ATP13A2* cDNA were amplified from whole blood of family members and control brain cDNA. The father and affected members show an aberrant amplicon of 368 bp in addition to the 479-bp WT product. Sequencing uncovers in-frame skipping of exon 13. (**d**) Predicted topology model of ATP13A2 showing the location and effect of KRS mutations. The position of frameshift mutations is indicated by red stars; the in-frame exon skipping is shown by red shading.

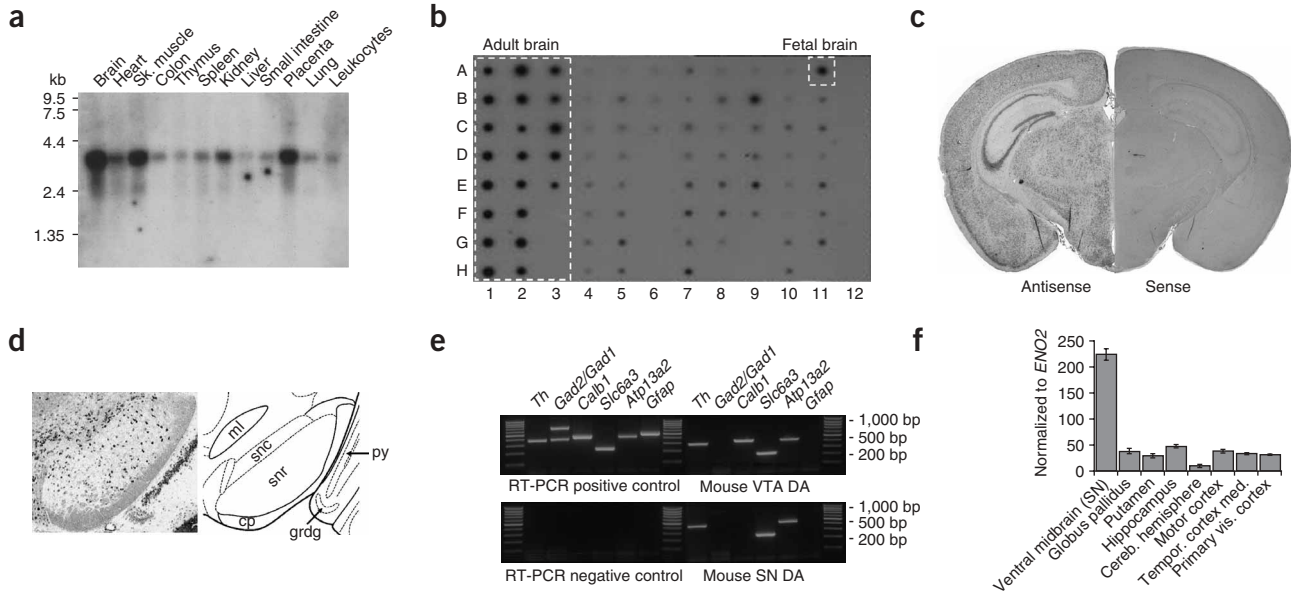

Figure 3 Expression analysis of *ATP13A2*. (**a**) Human multiple-tissue RNA and (**b**) dot blots (BD Biosciences Clontech) show ubiquitous *ATP13A2* expression with highest expression in brain and all tested brain subregions, including the substantia nigra (dot A3) and fetal brain (see also **Supplementary Fig. 2** online for control hybridization and **Supplementary Fig. 3** online for allocation of tissues on the dot blot). (**c**) *In situ* hybridization of adult mouse brain using a DIG-labeled antisense (left) or sense control probe (right) showing broad central nervous system expression of *Atp13a2*. (**d**) Larger magnification of a mouse *in situ* hybridization with an independent antisense probe (left) and schematic overview of the depicted brain region (right) shows a pronounced expression of *Atp13a2* in the substantia nigra pars compacta (snc). Cerebral peduncle (cp), granular layer of the dentate gyrus (grdg), medial lemniscus (ml), pyramidal cell layer of the hippocampus (py), substantia nigra pars reticularis (snr). (**e**) *Atp13a2* is expressed in individual mouse dopaminergic neurons from substantia nigra and ventral tegmental area (VTA). For laser-microdissected pools of individual cells, codetection was as follows: *Th*- and *Slc6a3*-positive cells (substantia nigra), *Atp13a2* codetection was 84% (10/12); for *Th*-, *Slc6a3*- and *Calb1*-positive cells, 100% (12/12). Note absence of glia or GABAergic contamination. For electrophysically characterized individual *Th*-positive neurons (substantia nigra), *Atp13a2* codetection was 87% (13/15); for *Th*- and *Calb1*-positive neurons (VTA), 100% (8/8), data not shown. (**f**) *ATP13A2* RNA levels (mean ± s.e.m.) in different human brain areas normalized to neuron-specific enolase (*ENO2*); $n = 3$ each. Highest expression is in ventral midbrain containing substantia nigra; lowest expression is in cerebellar hemisphere.

a protein of 1,180 amino acids. The gene covers 26 kb and 29 coding exons. *ATP13A2* is ubiquitously expressed as a 3.8-kb transcript, with strongest expression in brain (**Fig. 3a**). Dot blot analysis confirmed the predominant expression in human adult brain and demonstrated high expression in fetal brain and all tested subregions of the adult central nervous system (**Fig. 3b**), including the substantia nigra (signal A3 in **Fig. 3b**). To elucidate the spatial expression pattern, we performed *in situ* hybridization in adult mouse brain sections with two independent mouse *Atp13a2* antisense probes. Again, we found broad neuronal expression, including, for example, expression in the cortex and the thalamus (**Fig. 3c**) as well as the substantia nigra pars compacta (**Fig. 3d**).

We studied *ATP13A2* expression in individual dopaminergic midbrain neurons because of their crucial involvement in the etiology of parkinsonism and their essential role in voluntary movement and working memory. Using patch clamp–based harvesting or photoablation and laser microdissection systems, we isolated single dopaminergic neurons from mouse midbrain slices. We confirmed the identity of individual neurons by electrophysiology and molecular fingerprinting using single-cell PCR as previously described[17–19]. We used the expression profiles of marker genes to classify neurons as dopaminergic (if they were positive for tyrosine hydroxylase (*Th*) and dopamine transporter (*Slc6a3*, also known as *Dat*)) and to exclude a possible contamination by glial cells (using glial fibrillary acidic protein (*Gfap*)) and GABAergic neurons (using glutamate decarboxylase (*Gad2* (also known as *Gad65*) and *Gad1* (also known as *Gad67*)). We further subdivided dopaminergic neurons into calbindin (*Calb1*)-negative substantia nigra cells and calbindin-positive dopaminergic neurons from the neighboring ventral tegmental area (VTA). Qualitative PCR showed *Atp13a2* expression in pools of both substantia nigra and VTA dopaminergic neurons (**Fig. 3e**). Quantitative real-time RT-PCR experiments on total RNA from different human brain areas demonstrated the highest relative *ATP13A2* mRNA levels in ventral midbrain containing substantia nigra and lowest expression in the cerebellar hemisphere (**Fig. 3f**; relative *ATP13A2* mRNA expression normalized to *ENO2* ($n = 3$ each): ventral midbrain (containing substantia nigra), 223.8 ± 9.8; globus pallidus, 38.5 ± 0.4; putamen, 29.3 ± 1.4; hippocampus, 47.6 ± 1.4; cerebellar hemisphere, 10.2 ± 0.5; motor cortex, 39.3 ± 0.4; temporal cortex med., 33.8 ± 0.4; primary visual cortex, 31.3 ± 0.5).

We also investigated whether changes of *ATP13A2* expression were present in the common, sporadic forms of Parkinson disease by analyzing substantia nigra dopaminergic neurons from human post-mortem midbrains from individuals with idiopathic Parkinson disease and controls. By quantitative RT-PCR, we consistently detected about tenfold higher *ATP13A2* mRNA levels in selective pools (15 neurons each) of individual laser-microdissected tyrosine hydroxylase– and neuromelanin-positive substantia nigra dopaminergic neurons from brains of individuals with Parkinson disease than in comparable substantia nigra dopaminergic neurons from controls (**Fig. 4a–c**; relative *ATP13A2* mRNA expression in substantia nigra dopaminergic neurons: Parkinson disease brains ($n = 4$), 535 ± 47 (or for $n = 42$ pools, 544 ± 46); control brains ($n = 5$), 56 ± 12 (or for $n = 62$ pools, 48 ± 7); $P = 0.001$ for means analyzed brains (or $P = 1.6 \times 10^{-13}$ for

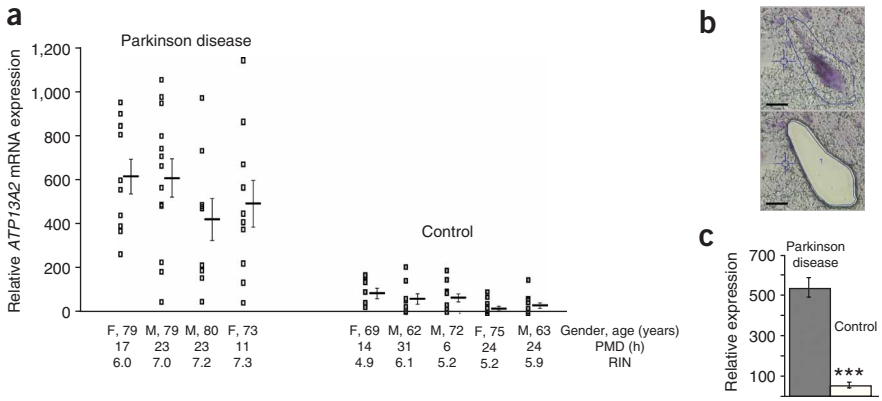

Figure 4 Expression analysis of *ATP13A2* mRNA levels in post-mortem brain samples of patients with idiopathic Parkinson disease and control individuals. (**a**) Scatter plot shows individual relative expression levels and mean (± s.e.m.) values of all analyzed substantia nigra dopaminergic pools (15 neurons each) for four different Parkinson disease brains and five controls. *ATP13A2* RNA levels are significantly higher in human TH- and neuromelanin (NM)-positive substantia nigra dopaminergic neurons from post-mortem Parkinson disease brains than in human substantia nigra dopaminergic neurons from post-mortem control brains. Age, gender, post-mortem delay (PMD) and RNA integrity number (RIN) of individual human midbrain samples are given for each brain (see also **Supplementary Table 3** and **Supplementary Fig. 1** for more details). (**b**) Individual substantia nigra dopaminergic neuron from human Parkinson disease brain SNRZ224 before and after laser microdissection (scale bar, 25 μm). (**c**) Relative expression of *ATP13A2* RNA (mean ± s.e.m.) for $n = 4$ Parkinson disease brains and $n = 5$ controls.

mean analyzed pools)). Agilent analysis of RNA quality indicated that RNA integrity was about 1.5 RNA integrity values (RIN) higher for brains from individuals with Parkinson disease compared with controls (5.4 ± 0.6 versus 6.9 ± 0.6 (mean ± s.d.), $P = 0.007$; see also **Supplementary Table 3** and **Supplementary Fig. 1** online). These RIN differences may account for a twofold overestimation of *ATP13A2* expression in Parkinson disease dopaminergic neurons for amplicons of 250–500 bp[20]. However, as we detected about tenfold higher *ATP13A2* mRNA levels with a TaqMan PCR assay of only 59 bp length, *ATP13A2* mRNA appears genuinely upregulated in surviving substantia nigra dopaminergic neurons in Parkinson disease.

To study the subcellular localization of ATP13A2, we heterologously expressed V5 epitope–tagged wild-type and KRS mutant protein in COS7 cells. After transient transfection, we observed a vesicular staining for wild-type protein, which colocalized with the lysosomal membrane proteins Lamp2 (**Fig. 5a**) and Lamp1 (data not shown). We did not observe colocalization with markers for mitochondria (by MitoTracker; **Fig. 5a**), endosomes, the exocytotic pathway or the Golgi apparatus (data not shown). We independently confirmed the lysosomal localization of ATP13A2 by confocal microscopy of a GFP-tagged wild-type construct and costaining with the intralysosomal marker LysoTracker (**Fig. 5b**). In contrast, the mutants showed a staining in a network-like structure (**Fig. 5c**). By costaining for protein disulfide isomerase (PDI), a marker for the endoplasmic reticulum, we demonstrated the accumulation of KRS mutants in the endoplasmic reticulum (**Fig. 5c**). This retention of truncated proteins in the endoplasmic reticulum supports the pathogenicity of KRS mutations on a cellular level. However, transient transfection and overexpression may lead to erroneous findings; therefore, these intracellular localization results will need to be confirmed by studies of the endogenous protein when specific ATP13A2 antibodies become available.

Erroneous and misfolded proteins are identified by the endoplasmic reticulum quality control and degraded by the proteasome[21]. To study

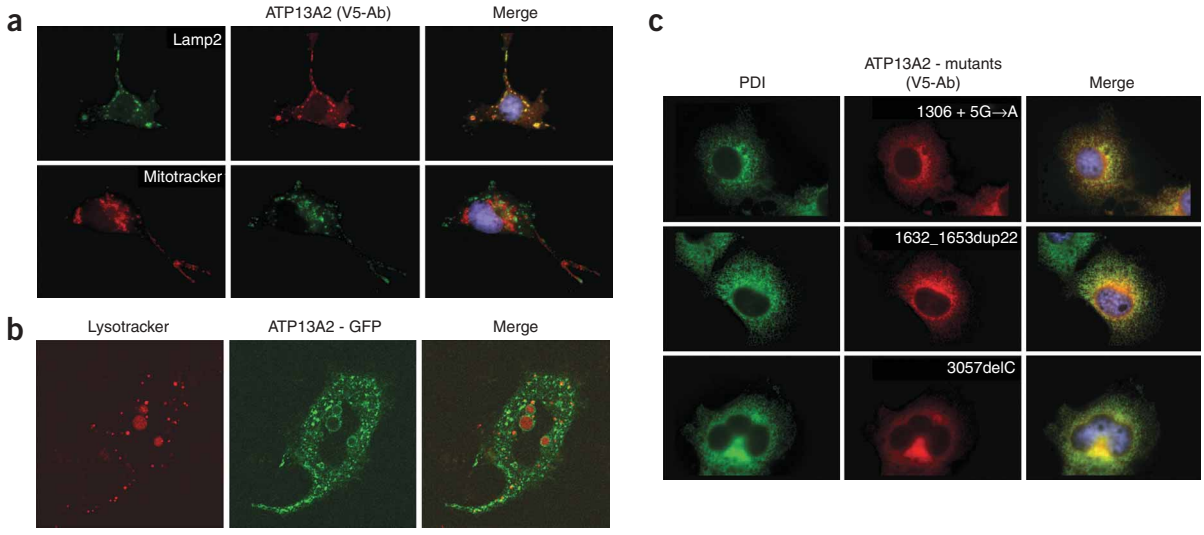

Figure 5 Subcellular localization of ATP13A2-WT and KRS-mutants in transiently transfected COS7 cells by immunofluorescence. (**a**) We observed colocalization between the V5-tagged wild-type construct and the lysosomal marker protein Lamp2 (top). For comparison, we did not find colocalization with the mitochondrial-specific dye MitoTracker Red (bottom). (**b**) The lysosomal localization of the wild-type protein was confirmed by colocalization of an ATP13A2/enhanced green fluorescent protein (EGFP) fusion protein with LysoTracker in transiently transfected COS7 cells. Note the intralysosomal staining for LysoTracker, whereas WT-ATP13A2-EGFP costains with the lysosomal membrane. (**c**) All KRS mutants are mislocalized and costain with the endoplasmic reticulum marker PDI (protein disulfide isomerase).

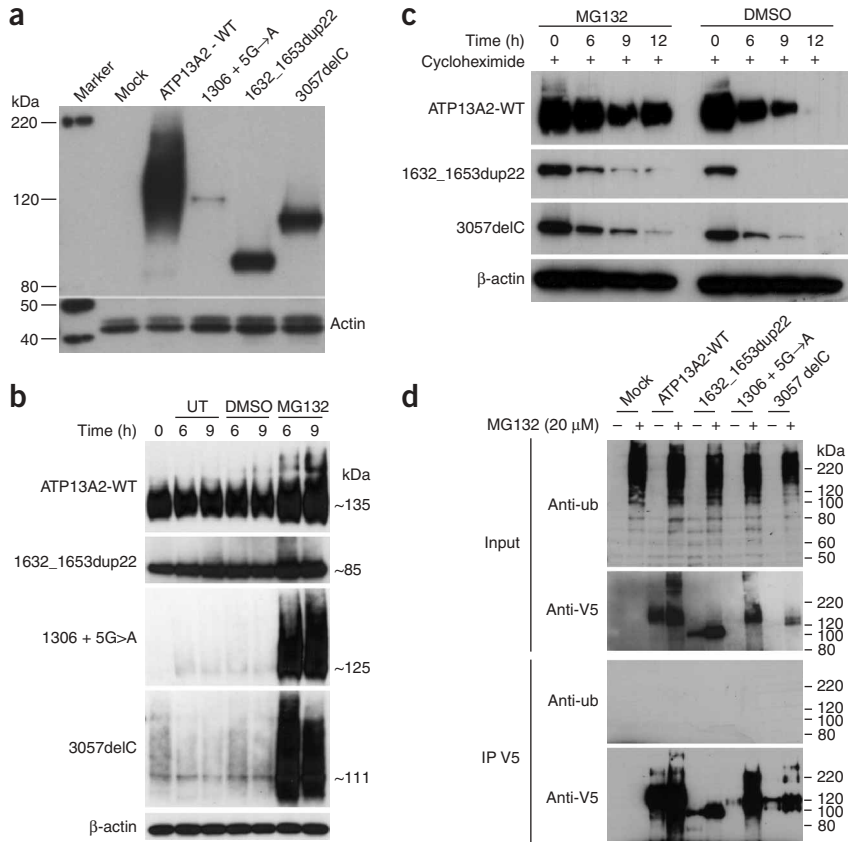

Figure 6 Protein blot analysis of ATP13A2 WT and mutant V5-tagged constructs in transiently transfected COS7 cells. (**a**) Immunoblotting shows a signal in the expected size range for all constructs. The stability of mutants is severely reduced compared with wild-type levels and the actin control (bottom). Note the lower amount of total protein in mock-transfected (vector pcDNA3.1 without insert) and wild-type–transfected samples. (**b**) The proteasomal inhibitor MG-132 (10 μM) stabilizes KRS mutants after 6 and 9 h, demonstrating the involvement of the proteasome in the degradation of KRS mutants. UT = untreated control cells. The estimated molecular weight in kDa is given at right. (**c**) Blocking of new protein synthesis in a cycloheximide (250 μg/ml) chase experiment (cell harvest after 6, 9 and 12 h) in the presence of MG-132 (10 μM) confirmed the involvement of the proteasome in the fast degradation of KRS mutants 1632_1653dup22 and 3057delC and the wild-type construct. DMSO-treated controls are shown at right. (**d**) Immunoprecipitation (IP) with V5 antibody shows no ubiquitylation of ATP13A2 wild-type or mutant constructs with or without MG-132 (20 μM) treatment but a specific signal with the V5-antibody (anti-V5). As a control, the input before immunoprecipitation is shown in the upper two panels with antibodies to ubiquitin (anti-ub) and V5.

a possible involvement of these systems, we performed protein blotting with transiently transfected COS7 cells. The wild-type protein showed a strong signal in the range of 130–140 kDa (predicted size, 129 kDa; **Fig. 6a**). Also, the three mutants showed bands in their predicted size ranges (125, 85 and 111 kDa for 1306+5G→A, 1632_1653dup22 and 3057delC, respectively; **Fig. 6a**). However, the quantities of the mutant proteins, particularly for 1306+5G→A, were severely diminished compared with wild-type protein and actin levels. Inhibition of the proteasome by MG-132 (10 μM) enhanced the stability of KRS mutants (**Fig. 6b**). Also, the wild-type protein was stabilized by MG-132, which was not seen in dimethylsulfoxide (DMSO)-treated or untreated control cells (**Fig. 6b**). We independently confirmed the involvement of the proteasome in the degradation of transfected KRS mutants (and ATP13A2 wild-type) in a cycloheximide (250 μg/ml) chase experiment (**Fig. 6c**). Although the DMSO-treated wild-type protein was completely degraded after 12 h of blocked protein synthesis, MG-132 (10 μM) strongly stabilized wild-type protein (**Fig. 6c**). We observed a similar stabilizing MG-132 effect for the KRS mutants 1632_1653dup22 and 3057delC (**Fig. 6c**). The KRS mutant 1306+5G→A was extremely unstable in the presence of cycloheximide even after 6 h (data not shown). We further tested whether the wild-type or mutant constructs were ubiquitylated in the presence or absence of MG-132 (20 μM; **Fig. 6d**) by immunoprecipitation with an antibody to V5. However, we could not detect ubiquitylation of the constructs (**Fig. 6d**, third panel). These results indicated that ATP13A2 may belong to the class of proteins such as ornithine decarboxylase and p21/Cip1 in which proteasomal degradation is ubiquitin independent[22,23]; however, further studies will have to analyze this in more detail.

A central theme in the pathogenesis of neurodegeneration is the disturbance of protein folding, aggregation and degradation[4–6]. There are two major pathways in proteolysis, the lysosome and the proteasome system[3]. Proteasomal dysfunction is a known cause of neurodegenerative disorders, and mutations in the gene encoding parkin[11] (an E3-ubiquitin ligase) cause a monogenic form of Parkinson disease. KRS mutations lead to protein retention in the endoplasmic reticulum and their enhanced proteasomal degradation. This may at least partially explain the neurodegeneration in KRS—for example, by proteasomal dysfunction owing to overload with mutant ATP13A2, which in turn might cause toxic aggregation. In addition, the putative lysosomal dysfunction by loss of ATP13A2 function may lead to insufficient lysosomal protein degradation. In fact, there is increasing evidence for an important role of the lysosome in the etiology of Parkinson disease, as demonstrated by the degradation of α-synuclein by autophagy[24,25] (and its impairment by Parkinson disease–associated α-synuclein mutations[26]) and the identification of mutations in the lysosomal glucocerebrosidase gene in individuals with Parkinson disease[27,28]. Whether loss of ATP13A2 function *per se* leads to a lysosomal dysfunction remains speculative, as functions and substrate specificities of all type 5 P-type ATPases are currently undefined[9]. However, our results linking ATP13A2 to the molecular pathophysiology of parkinsonism and dementia are likely to foster studies on this orphan class of proteins and will help to elucidate their function in the future.

METHODS

Clinical data. See **Supplementary Note**. All family members and parents (as legal guardians of affected individuals) gave their written informed consent. The study was approved by the hospital ethics committee of the University of Bonn.

Genotyping. We extracted genomic DNA from EDTA blood samples according to standard protocols. We selected microsatellite markers from candidate regions according to the Genethon and Marshfield maps and public data from

the human genome project (http://www.ensembl.org/ and http://genome.ucsc.edu/). We performed PCR amplification using standard protocols.

Linkage analysis. We analyzed the disease as an autosomal recessive trait with a mutant allele frequency of 0.001. We calculated two-point lod scores under the assumption of equal allele frequencies and using the computer MLINK program from the FASTLINK package version 5.1 (http://linkage.rockefeller.edu/soft/). We assumed recombination frequencies to be equal in male and female subjects and assumed allele frequencies to be $1/N$ (N = number of different alleles observed on the pedigree). We calculated nonparametric LOD scores using GENEHUNTER.

Mutation screening and cosegregation analysis. Using public databases, we selected candidate genes from the critical region. We delineated their genomic structure and developed a PCR-based testing strategy on genomic DNA. We amplified all exons by standard PCR on genomic DNA of one individual and one of the parents. We performed mutation analysis by direct sequencing of each amplicon. We deduced the genomic structure of *ATP13A2* using a human cDNA sequence from GenBank (NM_022089). Mutation numbering is based on a cDNA sequence from GenBank (NM_022089.1); position +1 corresponds to the A of the ATG translation initiation codon. Primer sequences are given in **Supplementary Table 2**. To confirm the predicted splicing effect of the 1306+5G→A mutation, we isolated total RNA from leukocytes from both parents, one unaffected family member and two affected individuals using TRIzol reagent (Invitrogen) according to the manufacturer's recommendations. We used approximately 1 µg of RNA to perform one-step RT-PCR experiments (Qiagen) according to the protocol supplied by the manufacturer.

Cloning of full-length cDNA of *ATP13A2*. We predicted the putative coding sequence of *ATP13A2* using public data from the human genome project (http://genome.ucsc.edu/). We designed overlapping primers according to the predicted cDNA sequence and performed PCR experiments on brain cDNA. We directly sequenced the amplicons to confirm the coding sequence and to detect possible splicing variants or polymorphisms. To confirm the putative start methionine, we performed 5′-RACE experiments on Marathon-Ready cDNA (BD Biosciences Clontech) according to the manufacturer's instructions.

Tissue distribution of ATP13A2. We first assayed *ATP13A2* expression by hybridization of a gene-specific probe located in the 3′ region of the cDNA. We amplified the probe from human brain cDNA using the primer pair cATP11F/ATP29R (**Supplementary Table 2**) and then radiolabeled the probe by random priming with [α-^{32}P]dCTP with the Ready-to-Go kit (Amersham Biosciences) using the protocol suggested by the manufacturer; we purified the labeled probe using a ProbeQuant G-50 Micro Column (Amersham Biosciences). We performed hybridizations using the 12-Lane Human Multiple Tissue Northern (MTN) Blot (BD Biosciences Clontech) and Human Multiple Tissue Expression (MTE) Array (BD Biosciences Clontech) according to the MTE protocol provided by the manufacturer. Briefly, both membranes were prehybridized for 30 min at 65 °C in ExpressHyb hybridization solution (BD Biosciences Clontech) containing denatured salmon testes DNA and then hybridized for 16 h at 65 °C with the labeled probe, which had been denatured in Cot-1 DNA (150 µg/ml; Roche Molecular Biochemicals), salmon testes DNA (750 µg/ml) and 4× SSC at 95 °C before being added to ExpressHyb. The MTE and MTN array were washed four times with 2× SSC/1% SDS at 65 °C, washed twice with 0.1× SSC/0.5% SDS at 55 °C and then developed on X-ray film at –70°C for 1 and 4 d.

***In situ* hybridization.** We linearized 1 µg of a pCR-II TOPO Dual vector (Invitrogen) containing a 554-bp *Atp13a2* PCR fragment, corresponding to the 3′-end of the mouse cDNA, with *Bam*HI or *Eco*RV to generate sense or antisense cRNA probes. The second independent probe is located in the coding region and was amplified with primers m13A22F and m13A22R (**Supplementary Table 2**). We performed *in vitro* transcription using the digoxigenin (DIG) RNA Labeling Kit (Roche) following the manufacturer's recommendations. We verified the integrity of the cRNA by electrophoresis on agarose gels. We performed *in situ* hybridization on paraffin-embedded 7-µm brain coronal sections from C57BL/6J mice. After deparaffinization and hydration of sections, we post-fixed the tissue to ensure attachment of sections to slides and incubated them in 1% H_2O_2 to block endogenous peroxidase. Tissues were permeabilized by proteinase K digestion and treatment with Triton X-100 and HCl. After triethanolamine treatment, samples were hybridized with 1 µl of probe per ml of hybridization buffer at 70 °C overnight. Specimens were then subjected to stringent post-hybridization washings. DIG detection was performed using alkaline phosphatase-conjugated antibodies to DIG (Roche) and BCIP/NBT.

Laser microdissection (LMD). We used a photoablation and laser microdissection system (PALM) for LMD of neurons from coronal cryosections of mouse midbrains. We used the LMD6000 system (Leica Microsystems) for human midbrain cryosections. We cut 12-µm sections (Leica cryostat CM1850), mounted them on RNase-free, ultraviolet light–treated membrane slides (1 mm PEN-membrane, PALM), fixed them with ethanol (75%, 95% 100%, 100%), stained them with cresyl violet in 100% ethanol and air-dried them. Neurons were visualized (63× objective), marked, cut and catapulted under bright-field illumination (DIC). From mouse, we analyzed individual neurons; from human sections, we collected and analyzed pools of 15 neuromelanin-positive neurons. Individual neurons were catapulted directly into tube lids (adhesive caps for PALM). The mixture for cell lysis (in 0.5% Nonidet P-40, Roche Diagnostics, and 20 U SUPERaseIn, Ambion) and cDNA synthesis was added directly into the lid. The tube was incubated upside down for 2 min at 72 °C and quickly cooled on ice before addition of reverse transcriptase.

RT-PCR. We performed electrophysiology, cytoplasm harvest, cDNA synthesis and qualitative and quantitative real-time single cell PCR as described previously[18,19]. Primer sequences for mouse calbindin (*Calb1*) D28k, tyrosine hydroxylase (*Th*), *Gfap* and *Gad2/Gad1* as described[17], primer sequences for *Atp13a2*, *Gad2/Gad1* and the dopamine transporter (*Slc6a3*) are given in **Supplementary Table 2**. Human total RNA from motor cortex, primary visual cortex, cerebellar hemisphere, globus pallidus, putamen, temporal medial cortex and hippocampus was purchased from Ambion. We isolated human ventral midbrain (including substantia nigra) from brain (Brain Bank Code SN 2/02) using the RNAeasy Mini kit (Qiagen). Human tissue RNA was reverse transcribed as described above. We used 5 µl of a 1:100 dilution for real-time PCR (20-µl reactions, duplicates, three independent runs each). We obtained human *post mortem* midbrain tissue from controls and individuals with Parkinson disease from the German BrainNet (http://www.brain-net.net/). After isolation of total RNA from midbrain cryosections (see above), we checked RNA integrity of individual human midbrains using Agilent analysis and by determining the RNA integrity number (RIN)[29,30]. For details on human brain samples, see **Supplementary Table 3**. Human real-time PCR assays were obtained from Applied Biosystems. ATP13A2 is an assay-by-demand (Hs00223032_m1, FAM/NFQ-labeled) amplifying a PCR product of 59 bp, and ENO2 is an assay-by-design (FAM/TAMRA-labeled) amplifying a PCR product of 108 bp (for *ENO2* primer sequences see **Supplementary Table 2**). All real-time PCRs of human LMD samples were analyzed at the same threshold (0.1). We calculated relative normalized expression according to $2^{(-\Delta Ct)} \times 100$. Relative expression of laser-microdissected human substantia nigra dopaminergic pools was given by $2^{(-Ct)} \times 10^{14}$. To evaluate statistical significance (normal parametric data), we performed Student's *t*-tests. A value of $P < 0.05$ was considered to be statistically significant and is indicated by asterisks. Data are given as mean ± s.e.m. if not otherwise stated.

Generation of plasmid constructs. We amplified the coding sequence of *ATP13A2* from brain cDNA with native *Pfu* DNA polymerase (Stratagene). The fragment was ligated into the mammalian expression vector pcDNA3.1/V5-His-TOPO (Invitrogen) and transformed into competent *Escherichia coli* TOP10 cells according to the manufacturer's instructions. We introduced disease-causing mutations in the wild-type construct through recombinant PCR. Owing to the early stop codons produced by 1632_1653dup22 and 3057delC mutations, we performed recombinant PCR to introduce the V5 epitope in-frame directly after the initial methionine. We confirmed integrity of all inserts by direct sequence analysis.

Cell culture, transfection and immunofluorescence. We maintained COS7 cells on Petri dishes or glass coverslips as monolayer cultures in DMEM containing 10% FCS (Invitrogen), 100 mg penicillin/ml, 100 units (U)

streptomycin/ml (Invitrogen) and amphotericin B (Fungizone) at 37 °C in an atmosphere of 5% CO_2/95% air. We performed transfections using Lipofectamine 2000 (Invitrogen) according to the manufacturer's protocol. Briefly, 24 h before transfection, cells were split in 60-mm Petri dishes at confluence of 80%–90% and kept in medium without antibiotics. The transfection was made using 6 μg DNA and 10 μl Lipofectamine 2000. For immunofluorescence, we cultured transiently transfected cells on glass coverslips for 24–48 h. We fixed the cells with ice-cold methanol:acetone (1:1) for 5 min at room temperature and permeabilized them with 0.1% Triton X-100 in PBS for 10 min at room temperature (25 °C). We prevented nonspecific binding with blocking solution (3% BSA in 1× PBS (Sigma)) for 30 min at room temperature. We detected ATP13A2 with antibody to V5 (Invitrogen) at a dilution of 1:500. We visualized endoplasmic reticulum and lysosomes through anti-PDI (Stressgen) and anti-H4B4 (DSHB) antibodies, respectively, at a dilution of 1:250. We directly labeled anti-V5 by Zenon Alexa Fluor 568 mouse IgG_{2a} kit and anti-PDI and anti-H4B4 by Zenon Alexa Fluor 488 Mouse IgG_1 kit (Molecular Probes) according to the manufacturer's instructions. Briefly, we incubated antibodies with the fluorophore-labeled Fc-specific anti-mouse IgG Fab fragment for 5 min (Zenon labeling complex formation). We blocked unbound fragments by adding Zenon blocking reagent for 5 min. We diluted freshly prepared Zenon labeling complex to a final dilution of 1:40 in blocking solution, applied it directly to the coverslips and incubated them at room temperature for 1 h. Coverslips were thoroughly washed in PBS for 5 min three times before fixation in 4% formaldehyde in 1× PBS for 10 min at room temperature. Coverslips were then washed twice with 1× PBS and mounted in antifade mounting medium containing DAPI (Vector Laboratories). Cells were imaged with a Zeiss Axioplan2 microscope with appropriate excitation and emission filter pairs. For mitochondrial labeling, we loaded cells before fixation with MitoTracker Orange CM-H_2TMROS (Molecular Probes) at a concentration of 0.5 ng/μl growth medium for 30 min at 37 °C. The staining for coverslips was carried out as described above, but the V5 antibody was labeled with the Zenon Alexa Fluor 488 Mouse IgG_{2a} kit. For confocal imaging, cells were transiently transfected with 3 μg of ATP13A2-EGFP plasmid on glass coverslips and 24 h after transfection were mounted in a perfusion chamber for observation. The cells were incubated with 100 nM LysoTracker Red DND-99 (Molecular Probes) for 10 min at room temperature, washed and analyzed with a Zeiss model LSM 510 confocal microscope equipped with argon (488 nm) and helium-neon (543 nm) lasers. The excitation of EGFP and LysoTracker was performed simultaneously by the 488 and 543 nm laser beam by a single-track function. We processed the images using Huygens Professional deconvolution software.

Protein blot analysis. We rinsed culture dishes once with cold PBS, collected cells in PBS and centrifuged samples at 16,100*g* for 10 min at 4 °C. We discarded the supernatant and resuspended the pellet in an appropriate amount of loading buffer (2× NuPAGE LDS Sample Buffer (Invitrogen) and 1× Complete Mini Protease Inhibitor Cocktail (Roche)) and made cell lysates using an ultrasonic bath. Volumes of 15 μl of each sample including 100 mM dithiothreitol (DTT) were boiled at 95 °C for 5 min and subjected to SDS-PAGE. After protein separation on 3–8% Tris-acetate or 4–12% Bis–Tris gels at 200 V for 45 min, we transferred proteins to PVDF membranes (Hybond-P; Amersham Biosciences) for 1 h at 32 V. We prevented nonspecific binding of antibody by blocking blots for 1 h with 2.5% low-fat dry milk in PBS containing 0.1% Tween 20 (PBST), followed by incubation in PBST with 2.5% low-fat dry milk including the primary antibody of choice in an appropriate concentration according to the manufacturer's suggestion with continuous rotation for 1 h at room temperature or overnight at 4 °C. The blots were washed for 15 min in PBST and subjected to PBST containing 2.5% low-fat milk and anti-rabbit and anti-mouse horseradish peroxidase-conjugated secondary antibodies (dilution 1:5,000). After 1 h incubation, blots were washed three times (20 min each wash) in PBST and visualized via an enhanced chemiluminescence kit (ECL) according to the manufacturer's suggested protocol (Pierce). Membranes were then exposed to X-ray film for 10 and 60 min. For semi-quantification of the amount of loaded protein, blots were incubated with anti-β-actin as a second primary antibody.

Immunoprecipitation. COS7 cells were transiently transfected with a mock construct (expression vector pcDNA3.1 (Invitrogen) without an insert) or the following V5-tagged constructs: wild-type, 1306+5G→A, 1632_1653dup22 and 3057delC. Cells were incubated for 12 h in DMEM alone or supplemented with 20 μM MG-132 (Calbiochem) and then subjected to immunoprecipitation. In brief, we rinsed culture dishes once with cold PBS, collected cells into PBS and centrifuged them at 16,100*g* for 5 min at 4 °C. We discarded the supernatant and resuspended the resulting pellet in 500 μl immunoprecipitation buffer (10% glycerol, 150 mM NaCl, 50 mM Tris (pH 7.4), 1% Igepal CA-630 (Sigma) and 1× Protease Inhibitor Cocktail (Roche)). Cells were lysed via ultrasonic water bath three times for 30 s each, followed by rotating end-over-end for at least 2 h at 4 °C. Samples were centrifuged at 16,100*g* for 10 min at 4 °C, and the supernatant was subdivided in three samples. The first one (input) consisted of 23 μl lysate that was mixed with 11.5 μl sample buffer, denatured for 5 min at 95 °C and stored at –20 °C for protein blot analysis. The remaining lysate was equally divided. One aliquot was incubated with mouse serum (negative control) and the other with 2 μg V5 antibody. Both samples were incubated at 4 °C overnight with end-over-end rotation. We added 60 μl of a suspension of Protein A–Sepharose Beads (Sigma) to the samples and rotated them end-over-end for 90 min at 4 °C. Then samples were centrifuged at 16,100*g* for 2 min at 4 °C, the resulting supernatant was discarded. The pellet containing the Protein A–Sepharose complex was washed three times with immunoprecipitation buffer. Finally, the samples were resuspended in 15 μl sample buffer and denatured for 5 min at 95 °C. Immunoprecipitates and inputs were resolved by SDS-PAGE and subjected to protein blot analysis using antibodies to V5 and ubiquitin.

Accession codes. GenBank: human *ATP13A2*, NM_022089; mouse *Atp13a2*, NM_029097; mouse *Gad2/Gad1*, NM_008078; mouse dopamine transporter, AF10907; human *ENO2*, NM_001975.

Note: Supplementary information is available on the Nature Genetics website.

ACKNOWLEDGMENTS

We thank E. Erxlebe and A. Cardenas for technical assistance, D. Isbrandt for help with the Agilent analysis and the families for their cooperation. Human brain samples were obtained from BrainNet (GA28). The antibody to H4B4 was obtained from the Developmental Studies Hybridoma Bank developed under the auspices of the National Institute of Child Health and Human Development (NICHD) and maintained by The University of Iowa Department of Biological Sciences. This study was supported by a grant of the Deutsche Forschungsgemeinschaft (DFG) to C.K. and grants from the Royal Society, the Bundesministerium für Bildung und Forschung (BMBF) (NGFN-2) and the Hertie Foundation to B.L. and J.R. C.G.W. is supported by the Wellcome Trust. CECS is a Millennium Science Institute and is funded in part by grants from Fundación Andes, the Tinker Foundation and Empresas Compañía Manufacturera de Papeles y Cartones (CMPC).

COMPETING INTERESTS STATEMENT

The authors declare that they have no competing financial interests.

1. Nussbaum, R.L. & Ellis, C.E. Alzheimer's disease and Parkinson's disease. *N. Engl. J. Med.* **348**, 1356–1364 (2003).
2. Vila, M. & Przedborski, S. Genetic clues to the pathogenesis of Parkinson's disease. *Nat. Med.* **10** (Suppl.), S58–S62 (2004).
3. Ciechanover, A. Proteolysis: from the lysosome to ubiquitin and the proteasome. *Nat. Rev. Mol. Cell Biol.* **6**, 79–87 (2005).
4. Cookson, M.R. The biochemistry of Parkinson's disease. *Annu. Rev. Biochem.* **74**, 29–52 (2005).
5. Dawson, T.M. & Dawson, V.L. Molecular pathways of neurodegeneration in Parkinson's disease. *Science* **302**, 819–822 (2003).
6. Selkoe, D.J. Cell biology of protein misfolding: the examples of Alzheimer's and Parkinson's diseases. *Nat. Cell Biol.* **6**, 1054–1061 (2004).
7. Najim al-Din, A.S., Wriekat, A., Mubaidin, A., Dasouki, M. & Hiari, M. Pallido-pyramidal degeneration, supranuclear upgaze paresis and dementia: Kufor-Rakeb syndrome. *Acta Neurol. Scand.* **89**, 347–352 (1994).
8. Williams, D.R., Hadeed, A., Al-Din, A.S., Wreikat, A.L. & Lees, A.J. Kufor Rakeb Disease: Autosomal recessive, levodopa-responsive parkinsonism with pyramidal degeneration, supranuclear gaze palsy, and dementia. *Mov. Disord.* **20**, 1264–1271 (2005).
9. Axelsen, K.B. & Palmgren, M.G. Evolution of substrate specificities in the P-type ATPase superfamily. *J. Mol. Evol.* **46**, 84–101 (1998).

10. Hampshire, D.J. *et al.* Kufor-Rakeb syndrome, pallido-pyramidal degeneration with supranuclear upgaze paresis and dementia, maps to 1p36. *J. Med. Genet.* **38**, 680–682 (2001).
11. Kitada, T. *et al.* Mutations in the parkin gene cause autosomal recessive juvenile parkinsonism. *Nature* **392**, 605–608 (1998).
12. Bonifati, V. *et al. DJ-1* (PARK7), a novel gene for autosomal recessive, early onset parkinsonism. *Neurol. Sci.* **24**, 159–160 (2003).
13. Valente, E.M. *et al.* Hereditary early-onset Parkinson's disease caused by mutations in *PINK1*. *Science* **304**, 1158–1160 (2004).
14. Kuhlbrandt, W. Biology, structure and mechanism of P-type ATPases. *Nat. Rev. Mol. Cell Biol.* **5**, 282–295 (2004).
15. Schultheis, P.J. *et al.* Characterization of the P5 subfamily of P-type transport ATPases in mice. *Biochem. Biophys. Res. Commun.* **323**, 731–738 (2004).
16. Kwasnicka-Crawford, D.A. *et al.* Characterization of a novel cation transporter ATPase gene (*ATP13A4*) interrupted by 3q25-q29 inversion in an individual with language delay. *Genomics* **86**, 182–194 (2005).
17. Liss, B., Neu, A. & Roeper, J. The weaver mouse gain-of-function phenotype of dopaminergic midbrain neurons is determined by coactivation of wvGirk2 and K-ATP channels. *J. Neurosci.* **19**, 8839–8848 (1999).
18. Liss, B. *et al.* Tuning pacemaker frequency of individual dopaminergic neurons by Kv4.3L and KChip3.1 transcription. *EMBO J.* **20**, 5715–5724 (2001).
19. Liss, B. Improved quantitative real-time RT-PCR for expression profiling of individual cells. *Nucleic Acids Res.* **30**, e89 (2002).
20. Schroeder, A. *et al.* The RIN: an RNA integrity number for assigning integrity values to RNA measurements. *BMC Mol. Biol.* **7**, 3 (2006).
21. Rao, R.V. & Bredesen, D.E. Misfolded proteins, endoplasmic reticulum stress and neurodegeneration. *Curr. Opin. Cell Biol.* **16**, 653–662 (2004).
22. Murakami, Y. *et al.* Ornithine decarboxylase is degraded by the 26S proteasome without ubiquitination. *Nature* **360**, 597–599 (1992).
23. Hoyt, M.A. & Coffino, P. Ubiquitin-free routes into the proteasome. *Cell. Mol. Life Sci.* **61**, 1596–1600 (2004).
24. Lee, H.J., Khoshaghideh, F., Patel, S. & Lee, S.J. Clearance of α-synuclein oligomeric intermediates via the lysosomal degradation pathway. *J. Neurosci.* **24**, 1888–1896 (2004).
25. Webb, J.L., Ravikumar, B., Atkins, J., Skepper, J.N. & Rubinsztein, D.C. α-synuclein is degraded by both autophagy and the proteasome. *J. Biol. Chem.* **278**, 25009–25013 (2003).
26. Cuervo, A.M., Stefanis, L., Fredenburg, R., Lansbury, P.T. & Sulzer, D. Impaired degradation of mutant α-synuclein by chaperone-mediated autophagy. *Science* **305**, 1292–1295 (2004).
27. Aharon-Peretz, J., Rosenbaum, H. & Gershoni-Baruch, R. Mutations in the glucocerebrosidase gene and Parkinson's disease in Ashkenazi Jews. *N. Engl. J. Med.* **351**, 1972–1977 (2004).
28. Goker-Alpan, O. *et al.* Parkinsonism among Gaucher disease carriers. *J. Med. Genet.* **41**, 937–940 (2004).
29. Auer, H. *et al.* Chipping away at the chip bias: RNA degradation in microarray analysis. *Nat. Genet.* **35**, 292–293 (2003).
30. Imbeaud, S. *et al.* Towards standardization of RNA quality assessment using user-independent classifiers of microcapillary electrophoresis traces. *Nucleic Acids Res.* **33**, e56 (2005).